One-Step Synthesis of TiO 2 /Graphene Nanocomposites by Laser Pyrolysis with Well-Controlled Properties and Application in Perovskite Solar Cells

Raphaëlle Belchi, Aurélie Habert, Eddy Foy, Alexandre Gheno, Sylvain Vedraine, ReMi Antony, Bernard Ratier, Nathalie Herlin-Boime, Johann Bouclé

ACS OMEGA

Article

Cite This: ACS Omega 2019, 4, 11906−11913

http://pubs.acs.org/journal/acsodf

One-Step Synthesis of TiO_2/Graphene Nanocomposites by Laser Pyrolysis with Well-Controlled Properties and Application in Perovskite Solar Cells

Raphaëlle Belchi,[†,‡] Aurélie Habert,[†] Eddy Foy,[†] Alexandre Gheno,[‡] Sylvain Vedraine,[‡] Rémi Antony,[‡] Bernard Ratier,[‡] Johann Bouclé,*[,‡] and Nathalie Herlin-Boime*[,†]

[†]NIMBE, CEA, CNRS, Université Paris-Saclay, CEA Saclay, 91191 Gif-sur-Yvette, France

[‡]Univ. Limoges, CNRS, XLIM, UMR 7252, F-87000 Limoges, France

Supporting Information

ABSTRACT: This work presents an original synthesis of TiO_2/graphene nanocomposites using laser pyrolysis for the demonstration of efficient and improved perovskite solar cells. This is a one-step and continuous process known for nanoparticle production, and it enables here the elaboration of TiO_2 nanoparticles with controlled properties (stoichiometry, morphology, and crystallinity) directly grown on graphene materials. Using this process, a high quality of the TiO_2/graphene interface is achieved, leading to an intimate electronic contact between the two materials. This effect is exploited for the photovoltaic application, where TiO_2/graphene is used as an electron-extracting layer in n−i−p mesoscopic perovskite solar cells based on the reference $CH_3NH_3PbI_{3-x}Cl_x$ halide perovskite active layer. A significant and reproducible improvement of power conversion efficiencies under standard illumination is demonstrated, reaching 15.3% in average compared to 13.8% with a pure TiO_2 electrode, mainly due to a drastic improvement in fill factor. This beneficial effect of graphene incorporation is revealed through pronounced photoluminescence quenching in the presence of graphene, which indicates better electron injection from the perovskite active layer. Considering that a reduction of device hysteresis is also observed by graphene addition, the laser pyrolysis technique, which is compatible with large-scale industrial developments, is therefore a powerful tool for the production of efficient optoelectronic devices based on a broad range of carbon nano-objects.

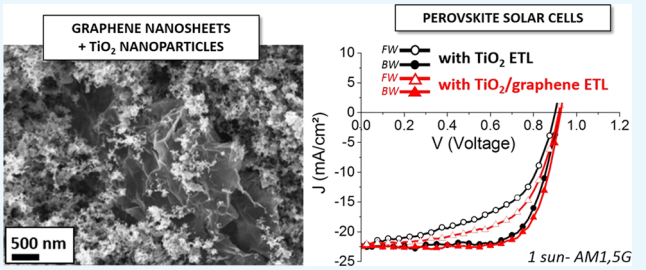

1. INTRODUCTION

The use of titanium dioxide (TiO_2) is nowadays widespread in many fields such as waste-water purification or photocatalysis due to its physical properties and chemical stability. In the field of sustainable energy, titanium dioxide has attracted more and more interest for rechargeable batteries, supercapacitors, photocatalytic hydrogen generation, and solar cells.[1,2] More particularly, at the nanometric scale, due to the critical contribution of active surfaces, TiO_2 offers interesting properties for many applications, and in particular for third-generation solar cells, such as dye-sensitized, organic, or perovskite solar cells.[3,4] In this field, a main limitation to current generation is associated with the recombination of excitons and/or charge carriers at many different levels. Therefore, regarding photogenerated electrons, the scientific community put many efforts to enhance the charge extraction layers of photovoltaic devices by synthesizing TiO_2-based thin films modified with metallic nanoparticles or carbon nanostructures.[5] In particular, since the development of new synthesis methods of graphene materials, TiO_2/graphene nanocomposites showed a strong potential to replace pure TiO_2 to reach optimal material properties for the photovoltaic application. Graphene materials are indeed now well known for their excellent conductive properties and high specific area, attracting strong interest for electronic applications.[6]

In the field of perovskite solar cells, high efficiencies of more than 23% have been recently reached,[7,8] but efforts remain to be performed to improve charge extraction, especially concerning the development of efficient and reliable charge transporting electrodes and selective contacts. The motivation for using TiO_2/graphene nanocomposites as a mesoporous electron transport layer aims at improving charge transfer and electron collection, thus leading to reduced charge trapping and recombination that can occur at the surface of titanium dioxide.[9−13] These benefits rely on the possibility for efficient electron transfer mechanisms from TiO_2 to graphene, as reported in the field of dye-sensitized solar cells.[14]

Among the numerous works reported over the last few years, the study carried by Nicholas et al. clearly demonstrates the benefit of TiO_2/graphene nanocomposites as an electron transport material in perovskite solar cells by reaching 15.6% power conversion efficiency (PCE) for the best cell using a

Received: May 13, 2019
Accepted: June 26, 2019
Published: July 9, 2019

DOI: 10.1021/acsomega.9b01352
ACS Omega 2019, 4, 11906−11913

Table 1. Main Features of TiO_2 and 0.04G/TiO_2 Annealed Powders Elaborated by Laser Pyrolysis

	production rate (g/h)	specific surface (g/m^2)	particle size (BET) (nm)	crystallinity (normalized intensity)			crystallite size (nm)
				anatase	rutile	srilankite	
TiO_2	2.8	63	25	1	0.17	0	15
0.04G/TiO_2	0.18	97	16	1	0.20	0.1	10

reference n−i−p device configuration.[15] One main benefit of the strategy is the possibility to achieve efficient TiO_2 electrode at low temperatures (<150 °C), although it requires several independent processing steps for the preparation of graphene, TiO_2, and the final nanocomposite.

Different pathways have been reported for the elaboration of TiO_2/graphene nanocomposites, such as the sonication of graphene and titanium dioxide dispersions. In this case, TiO_2 nanoparticles anchor onto the graphene layers, leading to partial covering and weak bonding between both materials.[16] Other alternatives reported in the literature include sol−gel and hydrothermal methods, where graphene oxide is reduced in presence of a titanium-based precursor or a solution containing dispersed TiO_2 nanoparticles.[16] To this date, these procedures cannot enable the elaboration of TiO_2−graphene composites with controlled properties for both TiO_2 and graphene materials while ensuring a strong interface between them and also leading to a high production yield.

In this work, we present a one-step and continuous synthesis method of TiO_2/graphene nanocomposites by laser pyrolysis. Indeed, the synthesis by laser pyrolysis of such nanocomposites is a continuous process that leads to a production rate of several grams per hour. Moreover, laser pyrolysis neither use any solvent nor require cleaning or washing steps, which are inevitable in most of the other way of production mentioned in the literature.[17,18] This singular technique enables the direct synthesis of well-controlled TiO_2 nanoparticles on graphene sheets. Relevance of this process has been previously demonstrated for TiO_2/carbon nanotube nanocomposite production, exhibiting an improved efficiency when used as active materials in solid-state dye-sensitized solar cells.[19] In this context, the present study focuses on the morphological and structural properties of the TiO_2/graphene nanocomposites synthesized by laser pyrolysis and their integration into mesoporous (or mesoscopic) n−i−p perovskite solar cells. A clear improvement of photovoltaic performance is related to the intimate contact between graphene and TiO_2 associated with the synthesis method, which is clearly beneficial to charge extraction.

2. RESULTS AND DISCUSSION

2.1. Physical Properties of the TiO_2 and TiO_2 Graphene Nanopowders. The synthesis of TiO_2/graphene nanocomposite has been performed in a one-step method by laser pyrolysis, as described in Section 4. This very fine technique enables a continuous production of nanoparticles that are obtained as powders.[20] Besides the excellent purity of the materials, laser pyrolysis can also provide high production rate (up to 3 g/h at lab scale) in the case of pure TiO_2 synthesis, with no graphene addition.[21] Characteristics of the obtained nanopowders (size, crystallinity) are tuned by the choice of experimental conditions (including laser power, reactor pressure, and gas flow rate).[22] We aim at producing particles as small as possible so that the specific surface, hence interfacial interactions, will be maximized. Experimental parameters have been carefully chosen to favor the production of anatase phase.[22] Pure TiO_2 nanoparticles were synthesized by laser pyrolysis as a reference material from pure titanium (IV) isopropoxide (TTIP). To produce TiO_2/graphene nanocomposites, 0.04 wt % reduced graphene oxide (rGO) was dispersed into TTIP using ultrasounds and the suspension was carried out to the laser beam. The obtained nanocomposite-based powder is then labeled as 0.04G/TiO_2.

These as-formed powders obtained from the laser pyrolysis are of gray color. This gray color is attributed to a significant amount of residual carbon phases (25%) due to the decomposition of the precursors (TTIP and C_2H_4). Therefore, annealing under air (6 h at 430 °C) was systematically performed to remove this carbon as it is known to alter the electronic properties of the obtained materials. The annealing temperature was carefully determined from thermogravimetric analysis, which is presented in the Supporting Information (Figure S1), to avoid graphene combustion while ensuring amorphous carbon elimination. After annealing, the color of powders turn to white, as depicted in Figure S2 in the Supporting Information.

The annealed powders were then thoroughly analyzed, and we especially focus here on two samples referred as TiO_2 and 0.04G/TiO_2 samples, whose main characteristics are presented in Table 1.

The morphologies of the powders have been first studied by scanning electron microscopy (SEM). Figure 1a shows an overview of the general aspect of the powders and confirms good homogeneity of the samples. Moreover, through meticulous analysis, we were able to distinguish graphene

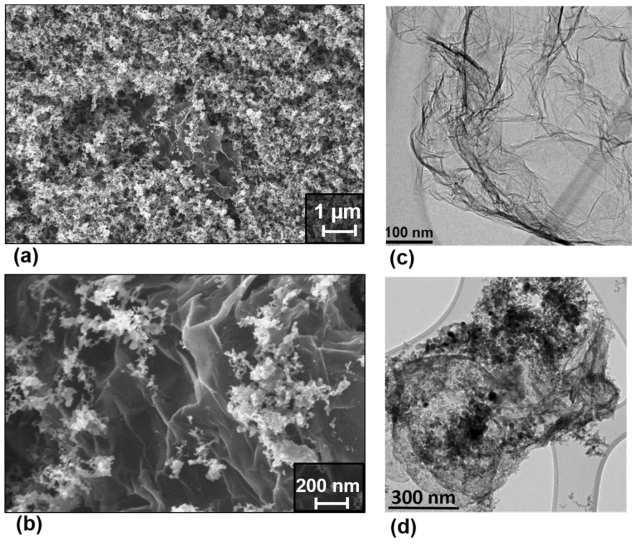

Figure 1. (a, b) SEM images of the TiO_2/graphene nanocomposite within the TiO_2 nanoparticle powder at different magnitudes. (c) TEM image of as-received graphene, before laser pyrolysis. (d) TEM images of the TiO_2/graphene nanocomposite obtained by laser pyrolysis (0.04G/TiO_2).

DOI: 10.1021/acsomega.9b01352
ACS Omega 2019, 4, 11906−11913

sheets within the TiO_2 matrix for sample 0.04G/TiO_2. Figure 1b shows a SEM image centered on a graphene sheet at a higher magnification. Within the powder, graphene is present in a small amount (considering that 0.04 wt % of graphene was introduced in the precursor mixture prior to the laser pyrolysis process) and is surrounded by TiO_2 nanoparticles; therefore, most of the TiO_2/graphene layers appear covered by a high amount of TiO_2 nanoparticles and cannot be easily seen through SEM characterization. Besides, TiO_2 particles seem to be very small as they reach the resolution limit of the microscope. Transmission electron microscopy (TEM) was therefore performed to get into more details.

Figure 1c shows the TEM image of as-received graphene, before laser pyrolysis. Its transparency emphasizes that only few carbon layers are involved, leading to very thin graphene sheets. This morphology seems to be preserved after the nanocomposite synthesis and after annealing, as shown in Figure 1d. As we can see, graphene is completely covered by TiO_2 nanoparticles, as one can only distinguish the edges of the graphene layer. For TEM observations, as mentioned in Section 4, the preparation of the microscope grids involves dispersion of the powders into ethanol using a high-power ultrasonic probe to separate the particles. Despite this treatment, a good coverage of graphene by titania particles is observed, which suggests a good quality of interface between the two materials. We highlight here that the quality of the interface between TiO_2 nanoparticles and carbon nanotubes synthesized by laser pyrolysis was already pointed out by our previous work,[19] which shows an intimate electronic contact between the two constituents. However, while carbon nanotubes are highly robust in terms of mechanical and thermal properties, graphene is much more sensitive to such stress. Achieving an intimate interface with TiO_2 without significantly altering the aspect of the graphene sheets is therefore an additional benefit of the laser pyrolysis process in our opinion, which remains difficult to achieve using other preparation methods.

In addition, complementary X-ray diffraction (XRD) measurements on the two powders are presented in Figure 2a, as well as their corresponding diffraction patterns.

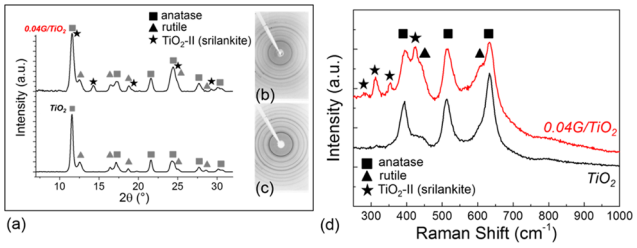

Figure 2. (a) XRD images of TiO_2 (pure TiO_2) and 0.04G/TiO_2 (TiO_2/graphene) nanopowders and (b), (c) their respective diffraction patterns (JCPDS card nos. 21-1272, 21-1276, and 84-1750). (d) Raman spectra of TiO_2 and 0.04G/TiO_2 focusing on the specific TiO_2 signatures.

For both materials, the major phase present is anatase, although a small fraction of rutile is also present (see Table 1). The average size of the crystallites is evaluated to be between 10 and 15 nm from Scherrer's equation,[23,24] showing that TiO_2 particles can be polycrystalline as the mean particle size evaluated by the Brunauer, Emmet and Teller (BET) method is around 20 nm (as reported in Table 1). A comparison of the two diagrams emphasizes the presence of several additional peaks in the 0.04G/TiO_2 nanocomposite. This phase can be attributed to the orthorhombic TiO_2-II phase, also named srilankite. This result is confirmed by Raman spectra recorded for pure TiO_2 and 0.04G/TiO_2 samples, as shown in Figure 2d. Besides the anatase signatures at 395, 516, and 634 cm^{-1}, clear signatures of srilankite TiO_2-II are evidenced at 282, 314, 354, and 424 cm^{-1} in the case of the 0.04G/TiO_2 sample. This phase is observed in all TiO_2/graphene nanocomposites produced using our laser pyrolysis process. Usually, the TiO_2-II is formed under high pressures and its structure is of the α-PbO_2 type. In this work, this phase is observed only when graphene is present in the reaction. We therefore assume that the presence of graphene, although in less amount, does change the synthesis conditions. Graphene would induce the creation of a reductive atmosphere that reduces a small fraction of anatase or rutile phase formed within the reactor during the laser pyrolysis. This TiO_2-II phase was also reported in another work[25] that uses a flame synthesis method to synthesize TiO_2 particles and produces a small fraction of TiO_2-II (srilankite) under oxygen-lean conditions. In addition, as graphene is not detectable by XRD, further information about the composite properties has been investigated by Raman scattering and is presented in the Supporting Information (Figure S3). The investigations performed by Raman spectroscopy confirm the presence of graphene within the nanopowders. They also show a significant increase of the D-to-G band ratio in the composite compared to that in pristine graphene, which suggests that defects have been introduced through the pyrolysis process or through close interactions of the graphene sheets with TiO_2 nanoparticles. This fact is consistent with the observations made by TEM.

We highlight here that these characterizations confirm the good crystallization of TiO_2 in the anatase form and the presence of graphene in our nanocomposites powder. Moreover, especially through TEM analysis, the interface between TiO_2 and graphene seems to be intimate, which is thus very promising for our application, as it can be associated with a good electronic contact.

2.2. From Powders to Mesoporous Electrodes.

Mesoporous TiO_2 and TiO_2/graphene electron transport layers were fabricated from the nanopowders synthesized by laser pyrolysis. A suspension of TiO_2 or TiO_2/graphene powder was prepared in ethanol at a weight ratio of 1:30 with regard to the solvent. Then, α-terpineol and ethyl-cellulose (previously dissolved in absolute ethanol) were added, following conventional recipes already published.[19,26] The obtained paste is sonicated for 1 h and stirred overnight before being spin-coated in air at 4000 rpm for 60 s and various substrates. The deposited films are then progressively annealed up to 430 °C to remove all of the organic components, leaving a high porosity and a mesoporous structure. Finally, the porous films are treated with $TiCl_4$ that is known to improve the surface states of nanostructured titania while improving the electronic percolation of adjacent particles, influencing consequently charge recombination and transport in the electrode (see the Supporting Information for experimental details).[27−30]

The main issue regarding the TiO_2/graphene composite is associated with the narrow thermal window that can be exploited for the post-sintering of the TiO_2 layers, required to remove the organic additives. The SEM cross section of the

DOI: 10.1021/acsomega.9b01352
ACS Omega 2019, 4, 11906−11913

mesoporous TiO_2/graphene layer obtained after sintering at 430 °C is presented in Figure 3a.

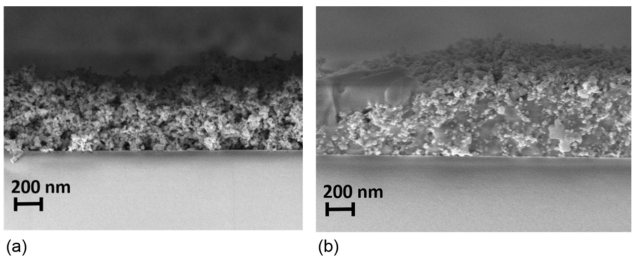

Figure 3. SEM cross section of the TiO_2/graphene mesoporous layer deposited on glass (a) before and (b) after perovskite ($CH_3NH_3PbI_{3-x}Cl_x$) infiltration.

The SEM image clearly demonstrates the achievement of a high-porosity film, similar to those generally reported using such recipes.[31,32] The absence of large aggregates is associated with a high transparency of the layers in the visible region (>90%) with almost no contribution from scattering, as observed by eye or through UV−visible transmission spectroscopy (Figure 4a). This observation is crucial to ensure that

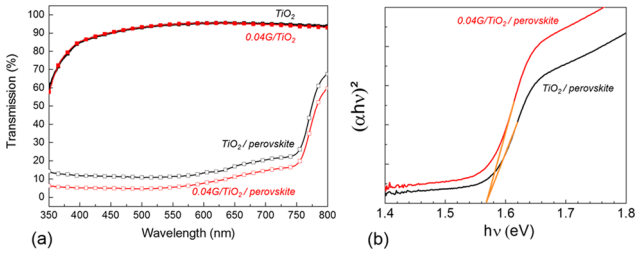

Figure 4. (a) UV−vis spectroscopy (transmission) of the mesoporous layer based on TiO_2 and 0.04G/TiO_2 powders and top-coated by perovskite. (b) Tauc's plot of TiO_2/perovskite and 0.04G/TiO_2/perovskite.

most of the incoming light reaches the perovskite material (the solar absorber) that will be infiltrated in the mesoporous electrode, as described in the next step.

We also note that the presence of graphene does not change the optical properties of our mesoporous layers, considering the low amount used here.

The $CH_3NH_3PbI_{3-x}Cl_x$ (MAPI-Cl) perovskite is deposited on top of this layer in a one-step process, described in Section 4 and Supporting Information (experimental details). Figure 3b shows that the pores of our TiO_2-based layers are well filled by the perovskite, ensuring a good interface between the two materials so that efficient electron injection can take place. UV−visible spectra of infiltrated TiO_2 and 0.04G/TiO_2-based mesoporous layers are reported in Figure 4a and shows the expected contributions of the metal oxide electrode and the perovskite layer (absorption edge close to 790 nm in our case). From this UV−visible spectra and using Tauc's equation (Figure 4b), the perovskite band gap is evaluated at 1.56 eV in both cases. We therefore assume that the presence of graphene does not significantly affect the perovskite crystallization.

Steady-state photoluminescence (PL) spectroscopy was conducted to better investigate the photoinduced charge transfer mechanisms at the TiO_2 layer/perovskite interface, as a function of the presence of graphene. A comparison was made with the pristine perovskite layer deposited on a mesoporous Al_2O_3 thin film, which acts as an insulating scaffold preventing any charge transfer process. A quenching of the perovskite photoluminescence emission (centered at 792 nm) is evidenced in the presence of a TiO_2-based electron transport layer, indicating that both TiO_2 and TiO_2/graphene materials can efficiently collect electrons photogenerated in the perovskite (Figure 5). Moreover, this quenching is significantly

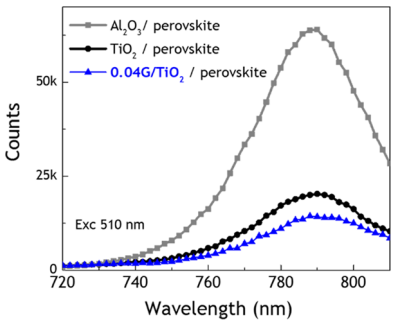

Figure 5. Steady-state photoluminescence spectroscopy: comparison of an electron-blocking layer (Al_2O_3) and an electron transport layer (TiO_2 and 0.04G/TiO_2).

enhanced in the presence of graphene, which indicates a better electron transfer efficiency compared to our pure TiO_2 reference. This observation is further confirmed through transient photoluminescence measurements presented in Figure S4 in the Supporting Information, which shows a significantly faster PL decay kinetics in the presence of graphene compared to pure TiO_2. Although there is still a debate in the literature about the relevance of mesoporous Al_2O_3 films as noninjecting reference substrates, the PL analysis clearly confirms that a better electronic interaction occurs between the perovskite and the graphene-loaded TiO_2 electrode compared to pure TiO_2.

2.3. From Mesoporous Electrodes to Photovoltaic Devices and Performance Measurements. Finally, the mesoporous TiO_2 layers, with and without graphene, were used as electron transport layers in perovskite solar cells using a glass-fluorine doped tin oxide (FTO)/dense TiO_2/mesoporous TiO_2 (without or with graphene)/MAPI-Cl perovskite/Spiro-OMeTAD/Au n−i−p architecture (see Figure S5b in the Supporting Information). A preliminary analysis on the influence of the graphene content in TiO_2 was conducted by adding cells containing an intermediate amount of graphene (0.02 wt %) for the comparison (the sample is labeled as 0.02G/TiO_2). Further details of the experimental procedure used for device preparation are reported in Section 4 and Supporting Information. Figure S5a presents the SEM cross section of a full device, showing that the expected sandwich structure is obtained.

Figure 6a−c represents typical current density−voltage (J−V) curves obtained from backward current−voltage characteristics measured under simulated solar emission (standard conditions, see experimental details in the Supporting Information) of perovskite solar cells based on TiO_2, 0.02G/TiO_2, and 0.04G/TiO_2 porous electrode. Table 2 presents the corresponding photovoltaic parameters (power conversion efficiency (PCE), short-circuit current density (J_{sc}), open-circuit voltage (V_{oc}), and fill factor (FF)), including those extracted from the forward J−V sweep. We emphasize that these parameters are average values obtained from a limited

DOI: 10.1021/acsomega.9b01352
ACS Omega 2019, 4, 11906−11913

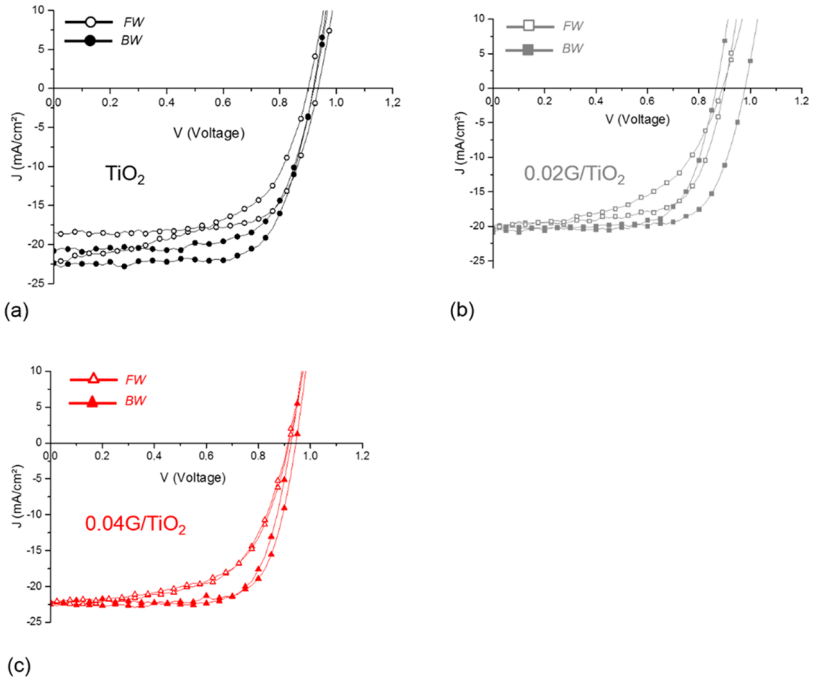

Figure 6. $J-V$ curves of solar cells with TiO_2 (a), $0.02G/TiO_2$ (b), and $0.04G/TiO_2$ (c) based electron transport layers.

Table 2. Photovoltaic Parameters Extracted from Forward and Backward Measurements and the Hysteresis Index of the Solar Cells

		PCE (%)	J_{sc} (mA/cm^2)	V_{oc} (V)	FF (%)	HI
FW	TiO_2	11.4 ± 1.2	20.6 ± 2.3	0.91 ± 0.3	61 ± 11	
	$0.02G/TiO_2$	10.6 ± 1.7	20 ± 0.2	0.89 ± 0	60 ± 10	
	$0.04G/TiO_2$	12.3 ± 0	22.3 ± 0.1	0.91 ± 0	61 ± 1	
BW	TiO_2	13.8 ± 1.2	21.7 ± 1.3	0.91 ± 0	70 ± 2	0.16 ± 0.06
	$0.02G/TiO_2$	13.2 ± 1.3	20.6 ± 0.2	0.92 ± 0.07	70 ± 0	0.09 ± 0.02
	$0.04G/TiO_2$	15.3 ± 0.1	22.3 ± 0.1	0.93 ± 0.01	74 ± 0	0.07 ± 0.02

number of devices that were processed in similar conditions for this study. It is important to note that the cells show significant hysteresis effect between forward and backward scans. This effect is mainly attributed to ionic migrations (mainly halides) in the perovskite layer, which can be directly affected by the charge extractions layers (either for electrons and holes).[33] Furthermore, it is also generally associated with interfacial defect states, as suggested by recent numerical simulation of perovskite solar cells.[34] Our mesoscopic device architecture, based on MAPI-Cl, is particularly sensitive to hysteresis as generally reported in the literature. Therefore, an adimensional hysteric index (HI), established by Sanchez et al., is also presented in Table 2.[35] HI is comprised between 0 (no hysteresis) and 1 (strong hysteresis).

In general, we clearly observe the improvement of solar cell performance with the increase of the graphene content. A high FF up to 74% (compared to 70% for the reference) and a decreased series resistance, from 26 to 22 Ω, are observed for cells containing graphene, evidencing a better charge extraction ability. In addition, the V_{oc} increases from 0.91 to 0.93 V and the short-circuit current density measured under standard illumination increases from 21.7 to 22.3 mA/cm^2 in the presence of graphene. This behavior is compatible with a better charge collection efficiency in the case of graphene-containing cells. This has a direct influence on power conversion efficiencies that reach an average of 15.3% efficiency compared to the 13.8% obtained for the reference. This trend is also confirmed through incident photon to charge carrier efficiency (IPCE) spectra measured on the devices, which are presented in the Supporting Information (Figure S6). The clear improvement of current generation over the whole spectral range is consistent with better charge extraction efficiency in the presence of the highest content of graphene (0.04 wt %).

Our results are consistent with the literature, for which an optimal graphene content exists.[15,36,37] Indeed, with a quite similar architecture of cell, Han et al. incorporated rGO into the mesoporous TiO_2 layer with three different concentrations (0.2, 0.4, and 1.0 vol %). The best content appeared to be the intermediate one (0.4 vol %) for which an efficiency of 13.5% was obtained, compared to the 11.5% of their reference cell (pure TiO_2).

Finally, the reduction of hysteresis in the case of TiO_2/graphene-based porous electrode is evidenced by the reduction of the HI by a factor 2. Zhang et al. pointed out the role of interfacial oxygen vacancies in TiO_2 as a potential cause of hysteresis in perovskite solar cells.[38] Our observations are therefore consistent with a reduction of oxygen vacancies on the TiO_2 particle surface by the introduction of graphene. The intimate contact induced by the laser pyrolysis process between TiO_2 and graphene is crucial in this context. Another positive influence of graphene incorporation is the fact that the standard deviation of all photovoltaic parameters is signifi-

DOI: 10.1021/acsomega.9b01352
ACS Omega 2019, 4, 11906−11913

cantly reduced for solar cells containing the 0.04G/TiO_2 composite material. Further in-depth analyses are currently undertaken to better interpret these effects; however, all of these indicators confirm the positive influence of graphene on perovskite solar cell operation.

Our first results are therefore very promising and clearly demonstrate the relevance of the laser pyrolysis process for the production of functional composites for energy conversion. Moreover, the optimal graphene content remains to be determined, suggesting that further performance improvement can be expected.

3. CONCLUSIONS

We show that laser pyrolysis enables to continuously produce TiO_2/graphene nanocomposites with controlled properties (such as TiO_2 crystallinity). More importantly, the technique provides an improved TiO_2−graphene interface and a coverage of the graphene sheets by the TiO_2 nanoparticles that induces a better electronic contact between them. Moreover, the technique can be expanded to produce one-step nanocomposites with different graphene contents or different graphene properties. The high quality of the obtained nanocomposites was applied to perovskite solar cells that exhibit a significant increase of their performance in average in the presence of graphene compared to pure TiO_2, as well as lower hysteresis. Moreover, these nanocomposites might be of interest for the study of aging or degradation of perovskite solar cells in which mesoporous TiO_2 is known to play an important role.[39,40] More generally, these results demonstrate the versatility of the laser pyrolysis process for the production of high-quality graphene nanomaterials and composites for solar energy conversion.

4. EXPERIMENTAL SECTION

To synthesize the nanocomposites, we choose a graphene material with suitable features for our application: a high conductivity and a few layers that offer a high specific area. Therefore, the "industrial G-200" material produced by the SIMBATT Company was used. Indeed, this industrial graphene powder is a reduced graphene oxide (rGO) with an oxygen content of less than 8 at.%, providing thus a high conductivity. Moreover, this graphene material is of a few layers (<10 layers), leading to a high specific area (>600 m^2/g). For convenience, we speak about graphene to mention this reduced graphene oxide (rGO). The titanium precursor is liquid and is the titanium (IV) isopropoxide 87560-500 ML (TTIP) purchased from Sigma-Aldrich (≥97% purity).

The synthesis of the TiO_2/graphene nanocomposite has been performed in a one-step method by laser pyrolysis. Its principle is based on the resonant interaction between a high-power infrared laser (CO_2) and a precursor mixture that can be either gas or liquid-nebulized microdroplets, carried into the reactor zone thanks to an inert gas (argon).[20] The TiO_2/graphene powders were obtained from TTIP as a liquid precursor for TiO_2 formation (a sensitizer gas, C_2H_4, is added to the carrier gas in this case, as TTIP does not absorb well the laser radiation at 10.6 μm) and our commercial few-layered reduced graphene oxide powder (SIMBATT, Shanghai, China). The CO_2 laser power was set to 520 W, and the pressure in the reactor was maintained at atmospheric pressure (10^5 Pa). Pure TiO_2 nanoparticles were synthesized by laser pyrolysis as a reference material from pure TTIP. To produce TiO_2/graphene nanocomposites, 0.04 wt % of reduced graphene oxide (rGO) was dispersed into TTIP using ultrasound. The obtained nanocomposite-based powder is then labeled as 0.04G/TiO_2.

The morphology of the powders were then evaluated by a Carl Zeiss ULTRA55 scanning electron microscope (SEM) and by a JEOL 2010 high-resolution transmission electron microscope (HRTEM) operated at 200 kV. For SEM analysis, the powder was directly observed on the carbon tape. For HRTEM measurements, the powder was dispersed in ethanol and nanoparticles were separated with intensive ultrasound irradiation using a Hielscher Ultrasound Technology ViAlTweeter UIS250V. Then, the dispersion was dropped on a grid made of a Lacey Carbon Film (300 mesh Copper, S166-3H).

The materials have been integrated into perovskite solar cells and tested under standard conditions (AM1.5G, 100 mW/cm^2) in ambiant atmosphere and without encapsulation to illustrate their quality and interest. Perovskite solar cells used in this work are composed of a stack of layers deposited onto glass substrates (see the structure in Figure S6). They comprise an FTO transparent electrode, followed by a compact TiO_2 acting as hole blocking layer, an electron transport mesoporous TiO_2 layer infiltrated by the perovskite, a hole transport Spiro-OMeTAD layer (doped with lithium salt (Li-TFSI) and *tert*-butylpyridine),[41] and finally a gold electrode. In this case, methylammonium lead iodide perovskite containing a small fraction of chlorine ($CH_3NH_3PbI_{3-x}Cl_x$, or MAPI-Cl) was deposited using a single-step procedure following a reported procedure.[42] This reference perovskite active layer was indeed found to allow a simple fabrication process in ambient conditions of devices with reasonable efficiencies due to the beneficial influence of chlorine on both charge diffusion length[43] and layer morphology and structure.[44] Further experimental features are detailed in the Supporting Information.

■ ASSOCIATED CONTENT

Supporting Information

The Supporting Information is available free of charge on the ACS Publications website at DOI: 10.1021/acsomega.9b01352.

Device preparation; X-ray diffraction analysis; Raman spectroscopy; steady-state and transient photoluminescence measurements; photovoltaic performance; complementary data regarding thermogravimetric analysis, Raman spectroscopy, transient photoluminescence, scanning electron microscopy, and IPCE measurements (PDF)

■ AUTHOR INFORMATION

Corresponding Authors

*E-mail: johann.boucle@unilim.fr (J.B.).
*E-mail: nathalie.herlin@cea.fr (N.H.-B.).

ORCID

Sylvain Vedraine: 0000-0002-0114-1599
Johann Bouclé: 0000-0002-7851-1842

Notes

The authors declare no competing financial interest.

DOI: 10.1021/acsomega.9b01352
ACS Omega 2019, 4, 11906−11913

■ ACKNOWLEDGMENTS

We are grateful for the financial support from IDEX Paris-Saclay and SigmaLim LabEX in Limoges. J.B. acknowledges the French Research National Agency (ANR) through the project "SuperSansPlomb" (ANR-15-CE05-0023-03). R.B., N.H.-B., and J.B. would like to thank Pierre-Eugène Coulon (Ecole Polytechnique/LSI/Palaiseau) for helpful support regarding transmission electron microscopy analysis and Marc Fabert (XLIM, CNRS, PLATINOM platforms at the University of Limoges) for helpful support regarding Raman experiments.

■ REFERENCES

(1) Lee, S-Y.; Park, S. TiO_2 photocatalyst for water treatment applications. *J. Ind. Eng. Chem.* **2013**, *19*, 1761−1769.
(2) Liu, Y.; Yang, Y. Recent progress of TiO_2-based anodes for Li-ion batteries. *J. Nanomater.* **2016**, *2016*, 1−15.
(3) Shen, S.; Chen, J.; Wang, M.; Sheng, X.; Chen, X.; Feng, X.; Mao, S. S. Titanium dioxide nanostructures for photoelectrochemical applications. *Prog. Mater. Sci.* **2018**, *98*, 299−385.
(4) Ge, M.; Cai, J.; Iocozzia, J.; Cao, C.; Huang, J.; Zhang, X.; Shen, J.; Wang, S.; Zhang, S.; Zhang, K.-Q.; Lai, Y.; Lin, Z. A review of TiO_2 nanostructured catalysts for sustainable H_2 generation. *Int. J. Hydrogen Energy* **2017**, *42*, 8418−8449.
(5) Bai, Y.; Mora-Séro, I.; De Angelis, F.; Bisquert, J.; Wang, P. Titanium Dioxide Nanomaterials for Photovoltaic Applications. *Chem. Rev.* **2014**, *114*, 10095−10130.
(6) Low, F. W.; Lai, C. W. Recent developments of graphene-TiO_2 composite nanomaterials as efficient photoelectrodes in dye-sensitized solar cells: A review. *Renewable Sustainable Energy Rev.* **2018**, *82*, 103−125.
(7) Yang, W. S.; Park, B.-W.; Jung, E. H.; Jeon, N. J.; Kim, Y. C.; Lee, D. U.; Seong, S. S.; Seo, J.; Kim, E. K.; Noh, J. H.; Seok, S. I. Iodide management in formamidinium-lead-halide-based perovskite layers for efficient solar cells. *Science* **2017**, *356*, 1376−1379.
(8) NREL Chart, 2019. https://www.nrel.gov/pv/cell-efficiency.html.
(9) Bouclé, J.; Herlin-Boime, N. The benefits of graphene for hybrid perovskite solar cells. *Synth. Met.* **2016**, *222*, 3−16.
(10) Acik, M.; Darling, S. B. Graphene in perovskite solar cells: Device design, characterization and implementation. *J. Mater. Chem. A* **2016**, *4*, 6185−6235.
(11) Hadadian, M.; Correa-Baena, J.-P.; Goharshadi, E. K.; Ummadisingu, A.; Seo, J.-Y.; Luo, J.; Gholipour, S.; Zakeeruddin, S. M.; Saliba, M.; Abate, A.; Grätzel, M.; Hagfeldt, A. Enhancing Efficiency of Perovskite Solar Cells via N-doped Graphene: Crystal Modification and Surface Passivation. *Adv. Mater.* **2016**, *28*, 8681−8686.
(12) Biccari, F.; Gabelloni, F.; Burzi, E.; Gurioli, M.; Pescetelli, S.; Agresti, A.; Del Rio Castillo, A. E.; Ansalado, A.; Kymakis, E.; Bonaccorso, F.; Di Carlo, A.; Vinattieri, A. Graphene-Based Electron Transport Layers in Perovskite Solar Cells: A Step-Up for an Efficient Carrier Collection. *Adv. Energy Mater.* **2017**, *7*, No. 1701349.
(13) Agresti, A.; Pescetelli, S.; Palma, A. L.; Del Rio Castillo, A. E.; Konios, D.; Kakavelakis, G.; Razza, S.; Cinà, L.; Kymakis, E.; Bonaccorso, F.; Di Carlo, A. Graphene Interface Engineering for Perovskite Solar Modules: 12.6% Power Conversion Efficiency over 50 cm^2 Active Area. *ACS Energy Lett.* **2017**, *2*, 279−287.
(14) Yang, N.; Zhai, J.; Wang, D.; Chen, Y.; Jiang, L. Two-Dimensional Graphene Bridges Enhanced Photoinduced Charge Transport in Dye-Sensitized Solar Cells. *ACS Nano* **2010**, *4*, 887−894.
(15) Wang, J. T.-W.; Ball, J. M.; Barea, E. M.; Abate, A.; Alexander-Webber, J. A.; Huang, J.; Saliba, M.; Mora-Sero, I.; Bisquert, J.; Snaith, H. J.; Nicholas, R. J. Low-Temperature Processed Electron Collection Layers of Graphene/TiO_2 Nanocomposites in Thin Film Perovskite Solar Cells. *Nano Lett.* **2014**, *14*, 724−730.
(16) Morales-Torres, S.; Pastrana-Martínez, L. M.; Figueiredo, J. L.; Faria, J. L.; Silva, A. M. T. Design of graphene-based TiO_2 photocatalysts — a review. *Environ. Sci. Pollut. Res.* **2012**, *19*, 3676−3687.
(17) Tho, N. T.; Mai, N. T. T.; Van, N. T.; Phat, B. D.; Hieu, L. V.; Thi, C. M.; Viet, P. V. Direct Synthesis of Reduced Graphene Oxide/TiO_2 Nanotubes Composite from Graphite Oxide as a High-Efficiency Visible-Light-Driven Photocatalyst. *J. Nanosci. Nanotechnol.* **2019**, *19*, 5195−5204.
(18) Atout, H.; Alvarez, M. G.; Chebli, D.; Bouguettoucha, A.; Tichit, D.; Llorca, J.; Medina, F. Enhanced photocatalytic degradation of methylene blue: Preparation of TiO_2/reduced graphene oxide nanocomposites by direct sol-gel and hydrothermal methods. *Mater. Res. Bull.* **2017**, *95*, 578−587.
(19) Wang, J.; Lin, Y.; Pinault, M.; Filoramo, A.; Fabert, M.; Ratier, B.; XBouclé, J.; Herlin-Boime, N. Single-step preparation of TiO_2/MWCNT nanohybrid materials by laser pyrolysis and application to efficient photovoltaic energy conversion. *ACS Appl. Mater. Interfaces* **2015**, *7*, 51−56.
(20) Cannon, W. R.; Danforth, S. C.; Flint, J. H.; Haggerty, J. S.; Marra, R. A. Sinterable Ceramic Powders from Laser-Driven Reactions: I, Process Description and Modeling. *J. Am. Ceram. Soc.* **1982**, *65*, 324−330.
(21) Curcio, F.; Musci, M.; Notaro, N.; De Michele, G. Synthesis of ultrafine TiO_2 powders by a CW CO_2 laser. *Appl. Surf. Sci.* **1990**, *46*, 225−229.
(22) Pignon, B.; Maskrot, H.; Guyot Ferreol, V.; Leconte, Y.; Coste, S.; Gervais, M.; Pouget, T.; Reynaud, C.; Tranchant, J.-F.; Herlin-Boime, N. Versatility of laser pyrolysis applied to the synthesis of TiO_2 nanoparticles - Application to UV attenuation. *Eur. J. Inorg. Chem.* **2008**, *2008*, 883−889.
(23) Klug, H. P.; Alexander, L. *X-ray Diffraction Procedures*, 2nd ed.; Wiley, 1974.
(24) Scherrer, P. Bestimmung der Grosse und der Inneren Struktur von Kolloidteilchen Mittels Rontgenstrahlen. *Nachr. Ges. Wiss. Goettingen* **1918**, 98−100.
(25) Wu, S.; Wang, W.; Tu, W.; Yin, S.; Sheng, Y.; Manuputty, M. Y.; Kraft, M.; Xu, R. Premixed Stagnation Flame Synthesized TiO_2 Nanoparticles with Mixed Phases for Efficient Photocatalytic Hydrogen Generation. *ACS Sustainable Chem. Eng.* **2018**, *6*, 14470−14479.
(26) Ito, S.; Murakami, T. N.; Comte, P.; Liska, P.; Grätzel, C.; Nazeeruddin, M. K.; Grätzel, M. Fabrication of thin film dye sensitized solar cells with solar to electric power conversion efficiency over 10%. *Thin Solid Films* **2008**, *516*, 4613−4619.
(27) O'Regan, B. C.; Durrant, J. R.; Sommeling, P. M.; Bakker, N. J. Influence of the $TiCl_4$ Treatment on Nanocrystalline TiO_2 Films in Dye-Sensitized Solar Cells. 2. Charge Density, Band Edge Shifts, and Quantification of Recombination Losses at Short Circuit. *J. Phys. Chem. C* **2007**, *111*, 14001−14010.
(28) Vesce, L.; Riccitelli, R.; Soscia, G.; Brown, T. M.; Di Carlo, A.; Reale, A. Optimization of nanostructured titania photoanodes for dye-sensitized solar cells: Study and experimentation of $TiCl_4$ treatment. *J. Non-Cryst. Solids* **2010**, *356*, 1958−1961.
(29) Adli, H. K.; Harada, T.; Nakanishi, S.; Ikeda, S. Effects of $TiCl_4$ Treatment on Structural and Electrochemical Properties of a Porous TiO_2 Layer in $CH_3NH_3PbI_3$ Perovskite Solar Cells. *Phys. Chem. Chem. Phys.* **2017**, *19*, 26898−26905.
(30) Abdi-Jalebi, M.; Dar, M. I.; Sadhanala, A.; Senanayak, S. P.; Giodano, F.; Zakeeruddin, S. M.; Grätzel, M.; Friend, R. H. Impact of Mesoporous Titania-Perovskite Interface on the Performance of Hybrid Organic-Inorganic Perovskite Solar Cells. *J. Phys. Chem. Lett.* **2016**, *7*, 3264−3269.
(31) Melhem, H.; Simon, P.; Beouch, L.; Goubard, F.; Boucharef, M.; Di Bin, C.; Leconte, Y.; Ratier, B.; Herlin-Boime, N.; Bouclé, J. TiO_2 Nanocrystals Synthesized by Laser Pyrolysis for the Up-Scaling of Efficient Solid-State Dye-Sensitized Solar Cells. *Adv. Energy Mater.* **2011**, *1*, 908−916.

DOI: 10.1021/acsomega.9b01352
ACS Omega 2019, 4, 11906−11913

(32) Schmidt-Mende, L.; Grätzel, M. TiO_2 pore-filling and its effect on the efficiency of solid-state dye-sensitized solar cells. *Thin Solid Films* **2006**, *500*, 296−301.
(33) Lee, H.; Gaiaschi, S.; Chapon, P.; Marronnier, A.; Lee, H.; Vanel, J.-C.; Tondelier, D.; Bourée, J.-E.; Bonnassieux, Y.; Geffroy, B. Direct Experimental Evidence of Halide Ionic Migration under Bias in $CH_3NH_3PbI_{3-x}Cl_x$-Based Perovskite Solar Cells Using GD-OES Analysis. *ACS Energy Lett.* **2017**, *2*, 943−949.
(34) Gheno, A.; Huang, Y.; Bouclé, J.; Ratier, B.; Rolland, A.; Even, J.; Vedraine, S. Toward Highly Efficient Inkjet-Printed Perovskite Solar Cells Fully Processed Under Ambient Conditions and at Low Temperature. *Sol. RRL* **2018**, *2*, No. 1800191.
(35) Sanchez, R. S.; Gonzales-Pedro, V.; Lee, J.-W.; Park, N.-G.; Kang, Y. S.; Mora-Sero, I.; Bisquert, J. Slow Dynamic Processes in Lead Halide Perovskite Solar Cells. Characteristic Times and Hysteresis. *J. Phys. Chem. Lett.* **2014**, *5*, 2357−2363.
(36) Han, G. S.; Song, Y. H.; Jin, Y. U.; Lee, J.-W.; Park, N.-G.; Kang, B.-K.; Lee, J.-K.; Cho, I. S.; Yoon, D. H.; Jung, H. S. Reduced Graphene Oxide/Mesoporous TiO_2 Nanocomposite Based Perovskite Solar Cells. *ACS Appl. Mater. Interfaces* **2015**, *7*, 23521−23526.
(37) Umeyama, T.; Matano, D.; Baek, J.; Gupta, S.; Ito, S.; Subramanian, V. R.; Imahori, H. Boosting of the Performance of Perovskite Solar Cells through Systematic Introduction of Reduced Graphene Oxide in TiO_2 Layers. *Chem. Lett.* **2015**, *44*, 1410−1412.
(38) Zhang, F.; Ma, W.; Guo, H.; Zhao, Y.; Shan, X.; Jin, K.; Tian, H.; Zhao, Q.; Yu, D.; Lu, X.; Lu, G.; Meng, S. Interfacial Oxygen Vacancies as a Potential Cause of Hysteresis in Perovskite Solar Cells. *Chem. Mater.* **2016**, *28*, 802−812.
(39) Mesquita, I.; Andrade, L.; Mendes, A. Perovskite solar cells: Materials, configurations and stability. *Renewable Sustainable Energy Rev.* **2018**, *82*, 2471−2489.
(40) Aristidou, N.; Sanchez-Molina, I.; Chotchuangchutchaval, T.; Brown, M.; Martinez, L.; Rath, T.; Haque, S. A. The Role of Oxygen in the Degradation of Methylammonium Lead Trihalide Perovskite Photoactive Layers. *Angew. Chem., Int. Ed.* **2015**, *54*, 8208−8212.
(41) Hawash, Z.; Ono, L. K.; Qi, Y. Recent Advances in Spiro-MeOTAD Hole Transport Material and Its Applications in Organic−Inorganic Halide Perovskite Solar Cells. *Adv. Mater. Interfaces* **2018**, *5*, No. 1700623.
(42) Gheno, A.; Thu Pham, T. T.; Di Bin, C.; Bouclé, J.; Ratier, B.; Vedraine, S. Printable WO_3 electron transporting layer for perovskite solar cells: Influence on device performance and stability. *Sol. Energy Mater. Sol. Cells* **2017**, *161*, 347−354.
(43) Stranks, S. D.; Eperon, G. E.; Grancini, G.; Menelaou, C.; Alcocer, M. J. P.; Leijtens, T.; Herz, L. M.; Petrozza, A.; Snaith, H. J. Electron-hole diffusion lengths exceeding 1 micrometer in an organometal trihalide perovskite absorber. *Science* **2013**, *342*, 341−344.
(44) Bouchard, M.; Hilhorst, J.; Pouget, S.; Alam, F.; Mendez, M.; Djurado, D.; Aldakov, D.; Schulli, T. U.; Reiss, P. Direct Evidence of Chlorine Induced Preferential Crystalline Orientation in Methylammonium Lead Iodide Perovskites Grown on TiO_2. *J. Phys. Chem. C* **2017**, *121*, 7596−7602.

DOI: 10.1021/acsomega.9b01352
ACS Omega 2019, 4, 11906−11913

Electronic Supporting Information of:

One-Step Synthesis of TiO_2/Graphene Nanocomposites by Laser Pyrolysis with Well-Controlled Properties and Application in Perovskite Solar Cells

Raphaëlle Belchi[1,2], Aurélie Habert[1], Eddy Foy[1], Alexandre Gheno[2], Sylvain Vedraine[2], Rémi Antony[2], Bernard Ratier[2], Johann Bouclé[2,*], Nathalie Herlin-Boime[1,*]

[1] *NIMBE, CEA, CNRS, Université Paris-Saclay, CEA Saclay 91191 Gif-sur-Yvette, France*

[2] *Univ. Limoges, CNRS, XLIM, UMR 7252, F-87000 Limoges, France*

* Corresponding authors: johann.boucle@unilim.fr; nathalie.herlin@cea.fr

Experimental Details

The compact TiO_2 layer is elaborated from a solution of titanium isopropoxide (TTIP, Sigma-Aldrich) in absolute ethanol (15.4 µL/mL). This one is deposited by spin-coating and annealed at 450°C for 20 min. Mesoporous TiO_2 and TiO_2/graphene electron transport layer of our solar cells were elaborated from the nanomaterials synthesised by laser pyrolysis. A solution was prepared with 190 µL of absolute ethanol, 43 µL of α –terpineol and 5 mg of the powder in which 100 mg of a solution of 40 mg ethyl-cellulose with 456 µL absolute ethanol was added. The obtained paste is sonicated for 1 hour and stirred during the night. It is then spin-coated at 4000 rpm for 60 seconds and the sample is annealed progressively up to 430°C to remove all organic components. Both TiO_2 layers are immerged into a bath of 220 µL $TiCl_4$ diluted into 100 mL of distilled water for 30 min at 70°C and annealed again at 450°C and 430°C respectively.

The solar absorber deposited on top of the mesoporous electron transport TiO_2 layer is a $CH_3NH_3PbI_{3-x}Cl_x$ perovskite. The precursor is a solution of 40 wt.% $PbCl_2$ and CH_3NH_3I with a molar ratio of 1:3, 59 wt.% of DMF and 1 wt.% 1,8-diiodooctane. The deposition of the perovskite is made in a single-step using spin-coating under nitrogen flow. The sample is then annealed at 90°C for 2 hours for an optimal crystallization. Further details on the experimental procedure used for device preparation are reported in the literature [1].

The crystalline phases of the materials were identified by X-Ray diffraction analysis (Rigaku Ru200BH) using a molybdenum anode (λ=0.70932 Å). Structural properties were probed by Raman spectroscopy using both a 633 nm red laser (LabRAM HR Evolution – Horiba) and a 532 nm green laser (XploRA PLUS – Horiba).

In addition, steady-state photoluminescence spectra were measured in the 720-850 nm range using FLS980 spectrometer (Edinburg Instruments, UK). The excitation (510 nm) is provided by a monochromated 450W Xenon lamp and the detection operated by a cooled R928P Hamamatsu photomultiplier. Quantitative measurements were obtained by normalizing the emission spectra by the effective fraction of light absorbed at the excitation wavelength, ensuring similar excitation conditions for all samples. Transient PL measurements were performed using the same apparatus equipped with picosecond laser diode emitting at 510 nm with a temporal width of 150 ps and a fast response photodetector. The detection was made through time-correlated single photon counting (TCSPC), and the traces were adjusted by taking into account the instrument response function (IRF), estimated using a diffusive reference sample.

Current density–voltage (J–V) characteristics were recorded in ambient conditions on un-capsulated devices (around 50% of relative humidity and in ambient air). A calibrated Keithley 2400 source-measure unit was used with a solar simulator (1600W NEWPORT) equipped with an AM1.5G filter. The spectral mismatch between the emission of the solar simulator and the global AM1.5G solar spectrum was taken into account using standard procedures (IEC 60904-9 Edition 2) and the solar simulator irradiance was corrected accordingly to match 100 mW cm^{-2} on the tested cell. The cells were masked with an aperture of 0.2 cm^2. Scan rates in the order of 80 $mV.s^{-1}$ were used as they were found to minimize the hysteresis effect in our conditions.

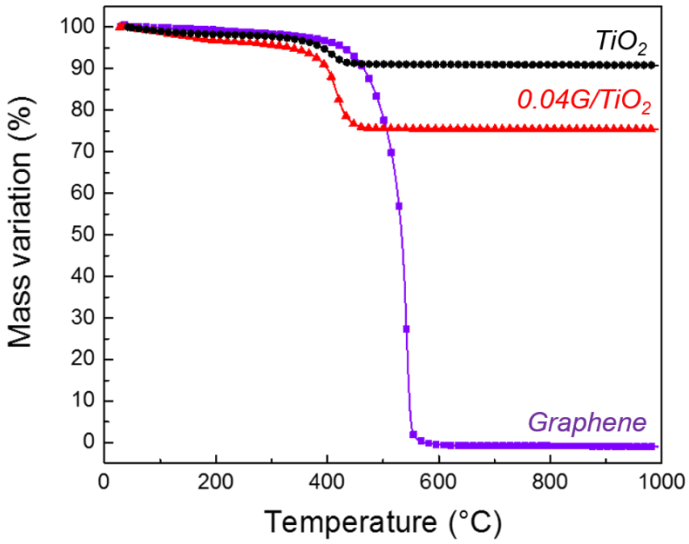

Figure S1 Thermogravimetric Analysis (TGA) of the pristine graphene and the powder obtained after laser pyrolysis: TiO_2 and 0.04G/TiO_2

Thermogravimetric Analysis (TGA) were conducted by heating the powders under air up to 1000°C (10°C/min). Graphene starts to be degraded from 450°C whereas amorphous carbon present in the TiO_2 and 0.04G/TiO_2 powders is eliminated after 400°C (cf. Figure S1). Therefore annealing treatment was fixed at 430°C to remove the undesirable carbon material.

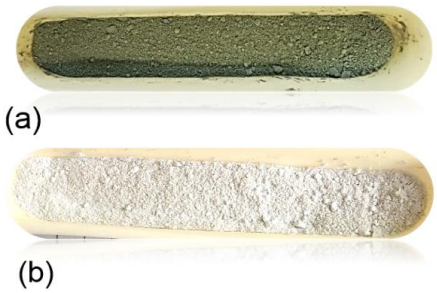

Figure S2 Aspect of a typical TiO_2/graphene nanopowder obtained by laser pyrolysis before (a) and after (b) thermal annealing at 430°C for 6h in air.

The darkened colour of the TiO_2-based powder after laser pyrolysis is due to the presence of the amorphous carbon (Figure S2 (a)). After removal of the carbon by annealing, the white characteristic colour of the TiO_2 is predominant (Figure S2 (b)).

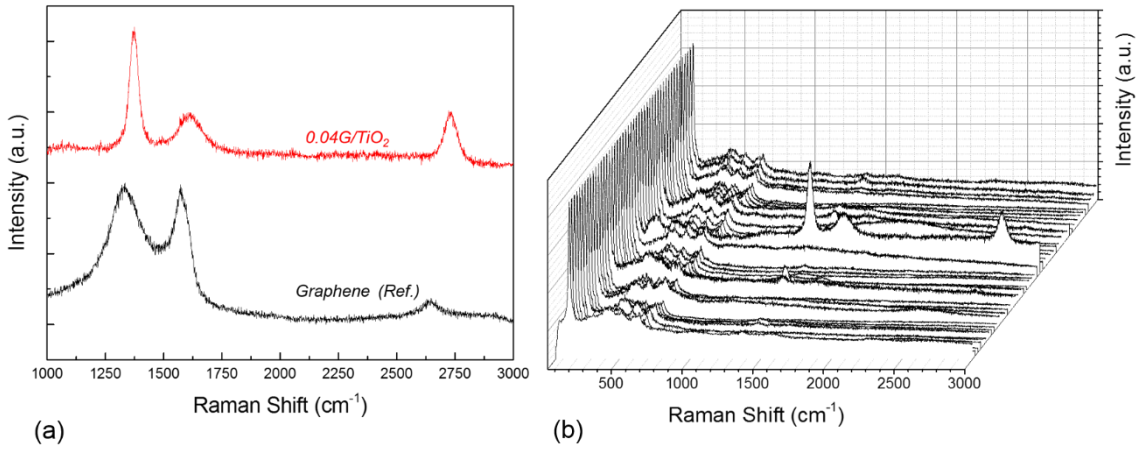

Figure S3 (a) Raman spectra showing carbon contributions of 0.04G/TiO_2 and pristine graphene (b) Raman spectra of 0.04G/TiO_2 after a mapping of 50 points

Figure S3 (a) shows the Raman spectra of the pristine graphene sample, which is compared to the carbon contributions recorded for our 0.04G/TiO_2 sample. The peaks located respectively at 1370 cm^{-1} and 1610 cm^{-1} are attributed to D and G bands of graphene whereas the 2D peak is observed around 2729 cm^{-1}.We observe a significant increase of the D band (disorder peak) with regard to pristine graphene: the intensity ratio between the D and G bands (I_D/I_G) increases up to 1.8 in the composite, whereas it is closer to 1 for the bare graphene alone. This observation is compatible with the introduction of defects by the pyrolysis process, and/or with the increase of the fraction of sp3 hybridization. This latter phenomenon could be consistent with the functionalization of graphene by the development of covalent bonds with the TiO_2 surface [1]. We also conducted Raman mapping of the 0.04G/TiO_2 annealed powder, presented in Figure S3 (b). This mapping is constituted of 50 points tested over an area of 450 μm^2 (the optical probe of our setup is around 1 μm^3). The mapping shows the good homogeneity of the sample and the large peak of anatase (at 146 cm^{-1}) is always dominant. In addition to the TiO_2 peaks, carbon contributions are observed on several measurement points and correspond to the signature of graphene.

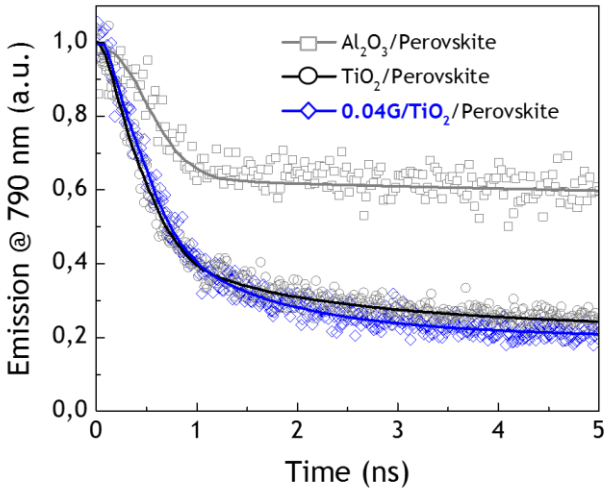

Figure S4 Transient photoluminescence (TRPL) : comparison of an electron blocking layer (Al_2O_3) and electron transport layer (TiO_2 and 0.04G/TiO_2)

Transient photoluminescence (TRPL) measurements are presented in Figure S4 and show a slightly faster PL decay kinetics in the presence of graphene compared to pure TiO_2. We note that a clear contribution of the mesoporous Al_2O_3 reference substrate is evidenced, as also reported in the literature[3].

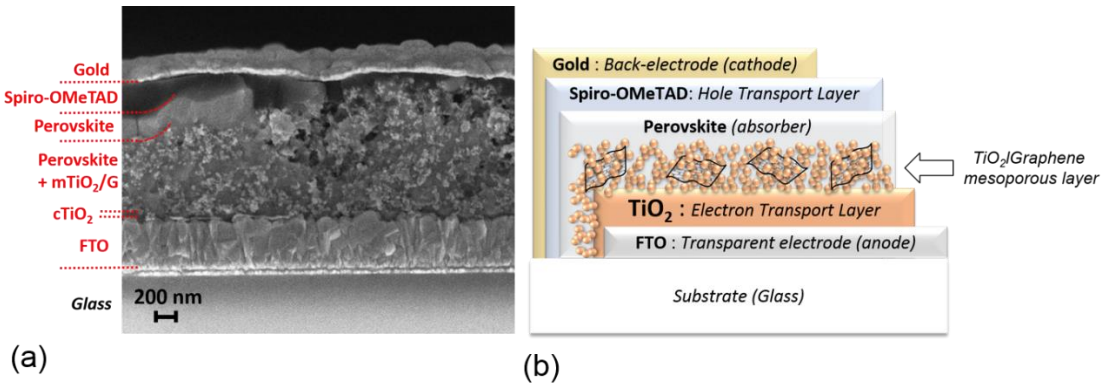

Figure S5 (a) SEM cross-section of a full perovskite solar cell (b) Perovskite solar cell architecture

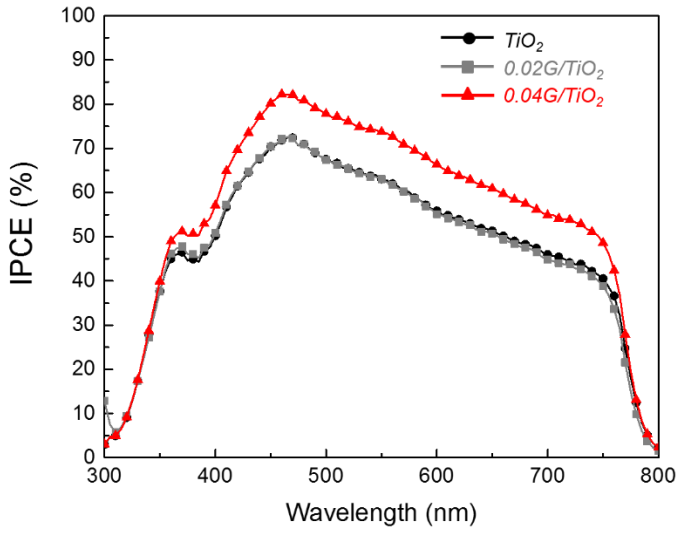

Figure S6 IPCE of perovskite solar cells with TiO_2, 0.02G/TiO_2 and 0.04G/TiO_2 based electron transport layers

Figure S6 presents typical IPCE measurements of perovskite solar cells based on TiO_2, 0.02G/TiO_2 and 0.04G/TiO_2 electron transport layers. Higher IPCE is reached for cells containing 0.04G/TiO_2, compared to the cells containing 0.02G/TiO_2 or pure TiO_2. We note that a slight decrease of the IPCE for longer wavelengths is in our case observed for all samples. This effect is associated with ion migration in the perovskite layer, which occurs over the duration of the measurement (several minutes) performed under low intensity monochromatic illumination (µW/cm²) and in short-circuit conditions, without any pre-biasing. Therefore, lower Jsc values than the ones extracted from J-V measurements under standard illumination have been estimated from IPCE curves (Jsc = 14 mA/cm² for the TiO_2-based solar cells, Jsc = 13.9 mA/cm² for 0.02G/TiO_2 and Jsc = 16.4 mA/cm² for 0.04G/TiO_2-based solar cells). Nevertheless, the general trend between samples is still observed through these measurements: a higher photo-current is obtained in case of 0.04G/TiO_2-based cells, highlighting the better charge collection efficiency upon adding of a certain fraction of graphene material in TiO_2.

Supporting information References

[1] A. Gheno, T. T. Thu Pham, C. Di Bin, J. Bouclé, B. Ratier, and S. Vedraine, "Printable WO3 electron transporting layer for perovskite solar cells: Influence on device performance and stability," *Sol. Energy Mater. Sol. Cells*, vol. 161, pp. 347–354, 2017.

[2] V. Georgakilas *et al.*, “Functionalization of graphene: Covalent and non-covalent approaches, derivatives and applications,” *Chem. Rev.*, vol. 112, no. 11, pp. 6156–6214, 2012.

[3] V. Roiati *et al.*, “Investigating charge dynamics in halide perovskite sensitized mesostructured solar cells,” *Energy Environ. Sci.*, vol. 7, no. 6, pp. 1889–1894, 2014.